Supplementary material for

Uniformizing the lithium deposition by gradient lithiophilicity and conductivity for stable lithium-metal batteries

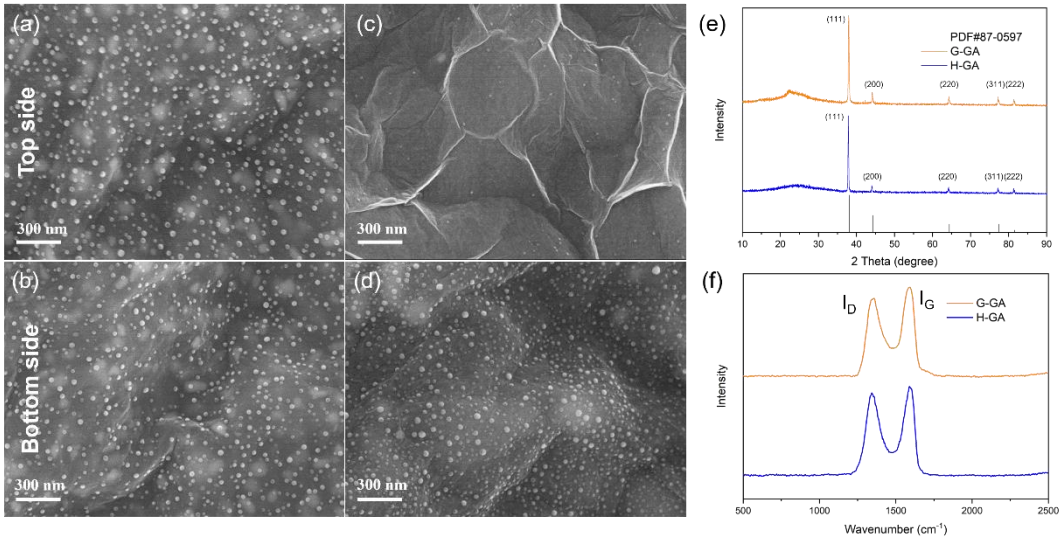

Figure S1. SEM characterization of H-GA and G-GA.(a-b) SEM images of top (a) and bottom (b) sides of H-GA.(c-d) SEM images of top (c) and bottom (d) sides of G-GA.(e) XRD patterns H-GA and G-GA films. Black drop lines represent the standard PDF #87-0597 for Ag crystal. (f) Raman spectra of H-GA and G-GA films.

Surface SEM images of gradient G-GA (Fig. S1c ~2d) show the similar morphology while both sides of H-GA (Fig. S1a~2b) have same AgNPs distribution trend of AgNPs. Both sides of H-GA are distributed Ag particles evenly. G-GA shows same structure of G-HGA where AgNPs barely occur on the top side. XRD pattens of G-GA and H-GA (Fig. S1e) showing diffraction peaks at 38.16°, 44.28°, 64.43°, 77.47°,

81.54° indicate (111), (200), (220), (311), (222) planes of Ag metal according to PDF #87-0597.Intensity ratios of D band to G band (I_D/I_G) of G-GA and H-GA are 0.876 and 0.919, respectively. Relatively high I_D/I_G of H-GA suggests the perturbation of AgNPs to carbon lattice array.

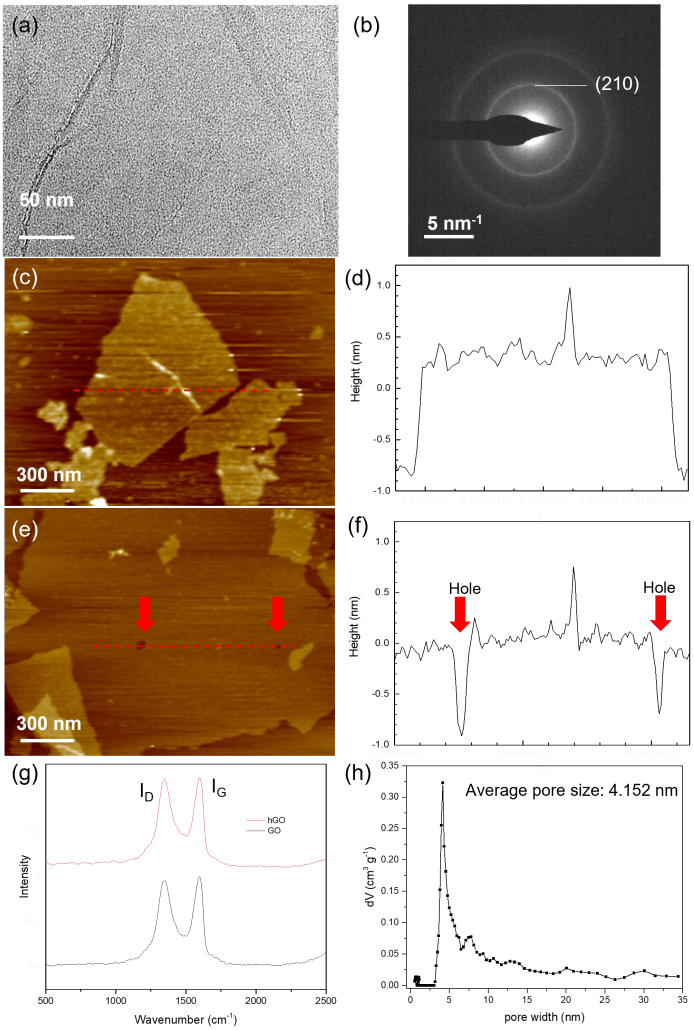

Figure S2. Characterizations of GO and hGO. (a-b) TEM image of (a) GO and corresponding (b) SEAD patterns (c-d) AFM images of (c) GO flake and (d) the height profile at red dash line in Fig. S2c (e-f) AFM images of (e) hGO flaks and (f) the height profile at red dash line in Fig. S2e.(g) Raman spectrum of GO and hGO. (h)Pore size distribution based on BJH method of hGO.

Instead of integrated 2D layer of GO (Fig. S2a), holes were observed on hGO, which could provide extra channels for Li^+ movement and promote ion transportation inside the gradient films. Structure difference of GO and hGO is also indicated by atomic force microscope (AFM) observation (Fig. S2c ~3f). Height profiles of red dash lines on the GO flake (Fig. S2c) and the hGO flake (Fig. S2e) are showed in Fig. S2d and Fig. S2f. Two sudden drops in Fig. S2f clearly exhibit the pores, further proving the existance of holes in hGO. The highest I_D/I_G of G-HGA among three samples (non-holy graphene or non-gradient film) indicates relatively high amounts of defects on the top side, further proved by Raman spectra of pure GO and hGO in Fig. S2g.

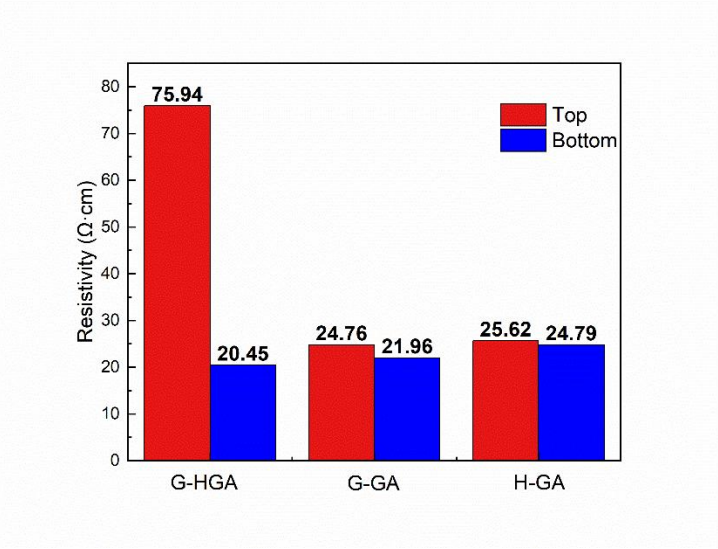

Figure S3. Top and bottom sides resistivity of the G-HGA, G-GA, H-GA film.

G-GA and H-GA have similar resistivities of both sides, which are 24.76 Ω·cm, 21.96 Ω·cm for G-GA and 25.62 Ω·cm, 24.79 Ω·cm for H-GA. Moreover, slight resistivity diversity of each side of G-GA and H-GA indicates that conductivity of composited film is mainly attribute to reduced GO substrate since most in-plane Ag nanoparticles distribute in isolation. Triple resistivity difference between top side (75.94 Ω·cm) and

bottom side (20.45 Ω·cm) of G-HGA helps reduce the top electrons density, thereby restricting top-growth Li deposition (Fig. S3).

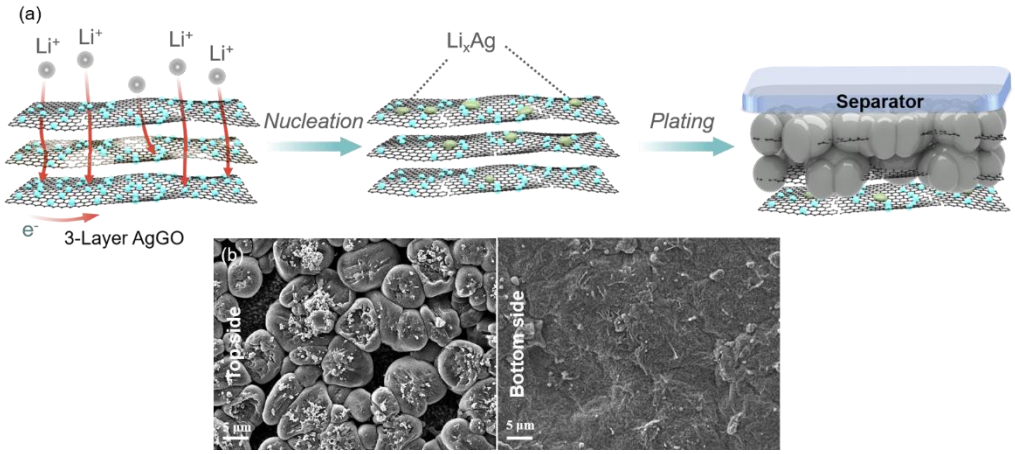

Figure S4. Li deposition behavior on the Hybrid AgGO (H-GA) film. (a) Schematic illustration of Li^+ plating behavior of H-GA film for Li-metal anodes. (b) SEM of top and bottom side of H-GA after plating 1 mAh cm^{-2}.

Spherical Li deposition was observed on the top surface of H-GA while AgNPs swelled to a lesser extent (Fig. S4b), showing the positive effect of Ag on suppressing Li dendrites. Nevertheless, the bottom side of H-GA carried small amount of Li proving that portable utilization of electrodes is hardly achieved by homogenization designs.

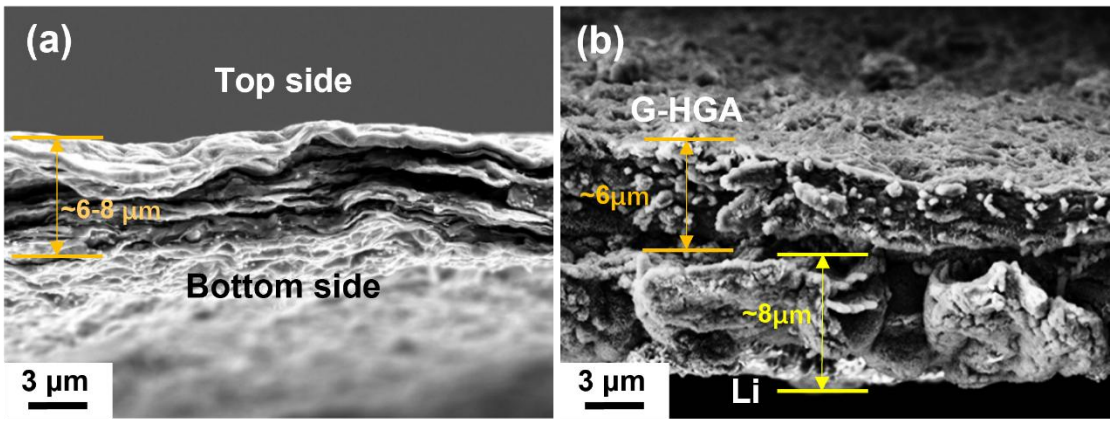

Figure S5. Cross-section view of (a) G-HGA film and (b) the deposited Li metal with Li = 2.0 mAh cm^{-2} lithium deposition at G-HGA film.

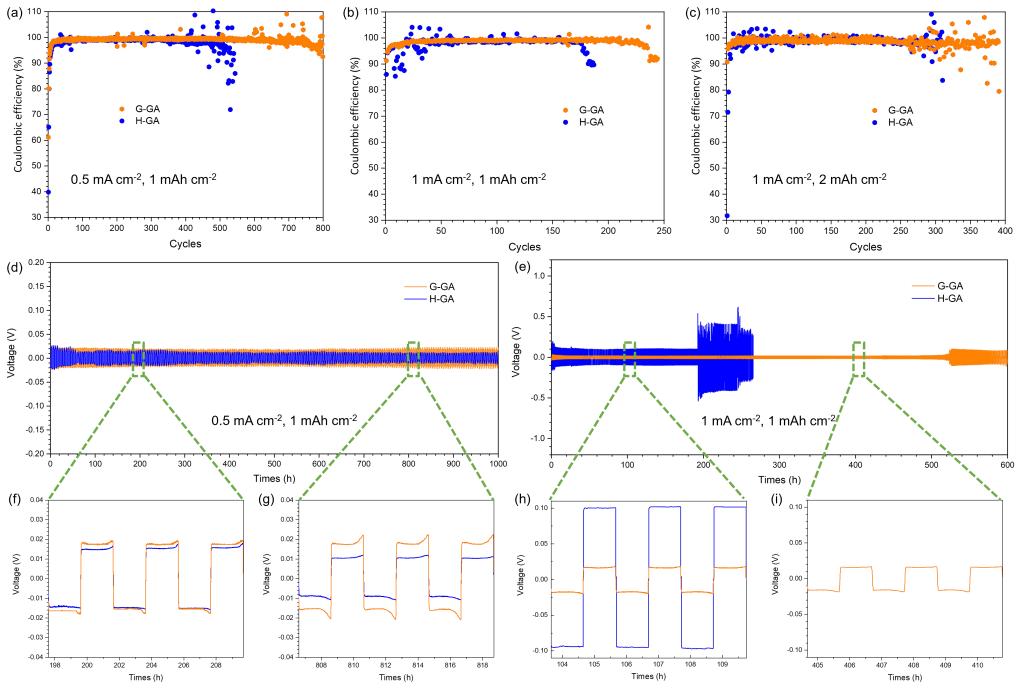

Figure S6. Electrochemical performance of H-GA and G-GA film. (a-c) Coulombic efficiency of half cells with H-GA and G-GA at (a) 0.5 mA cm^{-2}, 1 mAh cm^{-2}, (b) 1 mA cm^{-2}, 1 mAh cm^{-2} and (c)1 mA cm^{-2}, 2 mAh cm^{-2}. (d) Voltage profiles of symmetric cells with H-GA and G-GA at 0.5 mA cm^{-2}, 1 mAh cm^{-2}. Detailed voltage curve of (f) 50^{th} ~52^{th} cycles and (g) 200^{th} ~202^{th} cycles, respectively. (e) Voltage

profiles of symmetric cells with Cu and G-GA at 1 mA cm^{-2}, 1 mAh cm^{-2}. Detailed voltage curve of (h) 50^{th} ~52^{th} cycles and (i) 200^{th} ~202^{th} cycles, respectively.

The overpotential of G-GA@Li (~17 mV) is slightly larger than that of H-GA@Li (~11 mV), possibly resulting from bad ion mobility for Li^+ from the top surface to the deep H-GA film. The stability of H-GA is better than that of Cu but only maintained relatively stable for ~400 cycles at 0.5 mA cm^{-2}, 1 mAh cm^{-2}, 177 cycles at 1 mA cm^{-2}, 1 mAh cm^{-2} and 270 cycles at 1 mA cm^{-2}, 2 mAh cm^{-2}. Although spherical Li deposition can be achieved under the control of AgNPs on rGO matrix, further Li^+ hardly penetrates deep film and surface platting on H-GA is unavoidable. As more and more Li was discharged, H-GA gradually loses the control of Li dendrites from AgNPs and rGO matrix, leading to quick failure of LMAs. G-GA with gradient structure prolonged the life span to 798 cycles with CE higher than 90% at 0.5 mA cm^{-2}, 1 mAh cm^{-2}. When the current density increased to 1 mA cm^{-2}, G-GA||Li maintained steady CE over 242 cycles. Corresponding half cells cycling at 1 mA cm^{-2}, 2 mAh cm^{-2} showed less fluctuations compared to H-GA but failed around 270 cycles (Fig. S6j ~6l). Gradient G-GA and G-HGA prolong the life span to at least 600 h at 1 mA cm^{-2}, 1 mAh cm^{-2}. However, G-GA@Li showed a potential instability at 522 h with increasing voltage hysteresis of 180 mV, suggesting the undesirable dendrites formation.

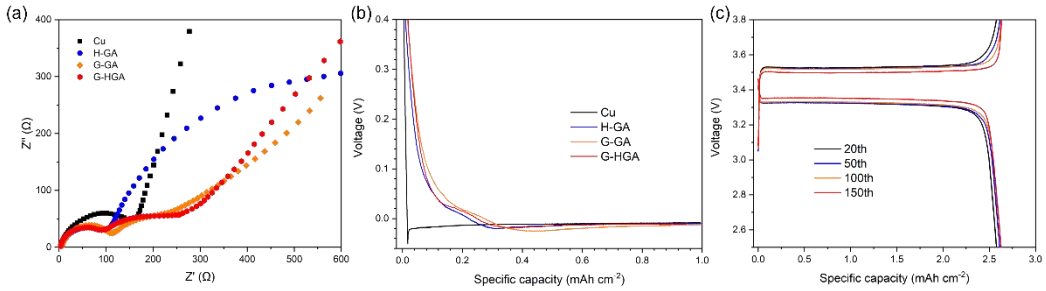

Figure S7. Electrochemical characterization of G-HGA and counter anodes. (a) EIS of half cells after 2 cycles using Cu, H-GA, G-GA and G-HGA as anodes respectively. (b) Voltage-capacity profiles of Cu, H-GA, G-GA and G-HGA at 0.1 mA cm^{-2} ,1 mAh cm^{-2}. (c) Voltage-capacity profiles of LFP||G-HGA@Li (N/P=1.13) in the ether-based electrolyte.

Electrochemical impedance spectrum (EIS) of G-HGA, G-GA, H-GA and Cu foils after two cycles at 1 mA cm^{-2}, 1 mAh cm^{-2} were also conducted to analyze nucleation and ion transport condition (Fig S7.a). Expect for Cu, EIS curves of composited graphene films show two apparent circles representing impedance of lithium nucleation and SEI layer, respectively. The interphase nucleation impedance of Cu ($\approx$180 Ω) is much higher than G-HGA ($\approx$50 Ω) because of lithiophobic nature of Cu with Li-metal. The interphase nucleation impedance of H-GA and G-GA 53 Ω and 59 Ω, respectively (Fig S7a). G-HGA shows faster ion movability than G-GA as indicated by the large slope of straight line in the end, demonstrating the positive influence of hGO on Li^+ movement. The larger impedances of Cu foil electrodes before and after the rate performance test suggest that uneven Li plating/stripping results in poor interface conductivity and slow ion transport. Besides EIS,

voltage-capacity profile could also indicate the deposition behavior of Li^+ on anodes materials. A typical charging profile is composed of a voltage drop with a following flat voltage plateau. Voltage difference between the bottom of the drop and the flat plateau represents nucleation overpotential of Li-metal plating on specific materials. Fig. S7b shows the voltage-capacity profile of G-HGA, G-GA, H-GA and Cu foil at 0.1 mAh cm^{-2}, 1mAh cm^{-2}. The overpotential for Li-metal on bare Cu is around 21 mV, indicating the bad wettability between Cu and Li. Three Ag composited graphene films represent similar voltage profile with two mild curve turns, manifesting the formation of different state Ag–Li alloy. G-HGA shows the smallest overpotential around 2 mV compared to 4 mV for H-GA and 6 mV for G-GA. Moreover, the second flat plateau of G-GA occurs at larger discharge capacity (0.44 mAh cm^{-2}) than that of G-HGA (0.32 mAh cm^{-2}) and H-GA (0.3 mAh cm^{-2}), indicating large barrier from top rGO layer of G-GA on Li^+ movement and the successful improvement of Li^+ transportation by introducing hGO to gradient films.

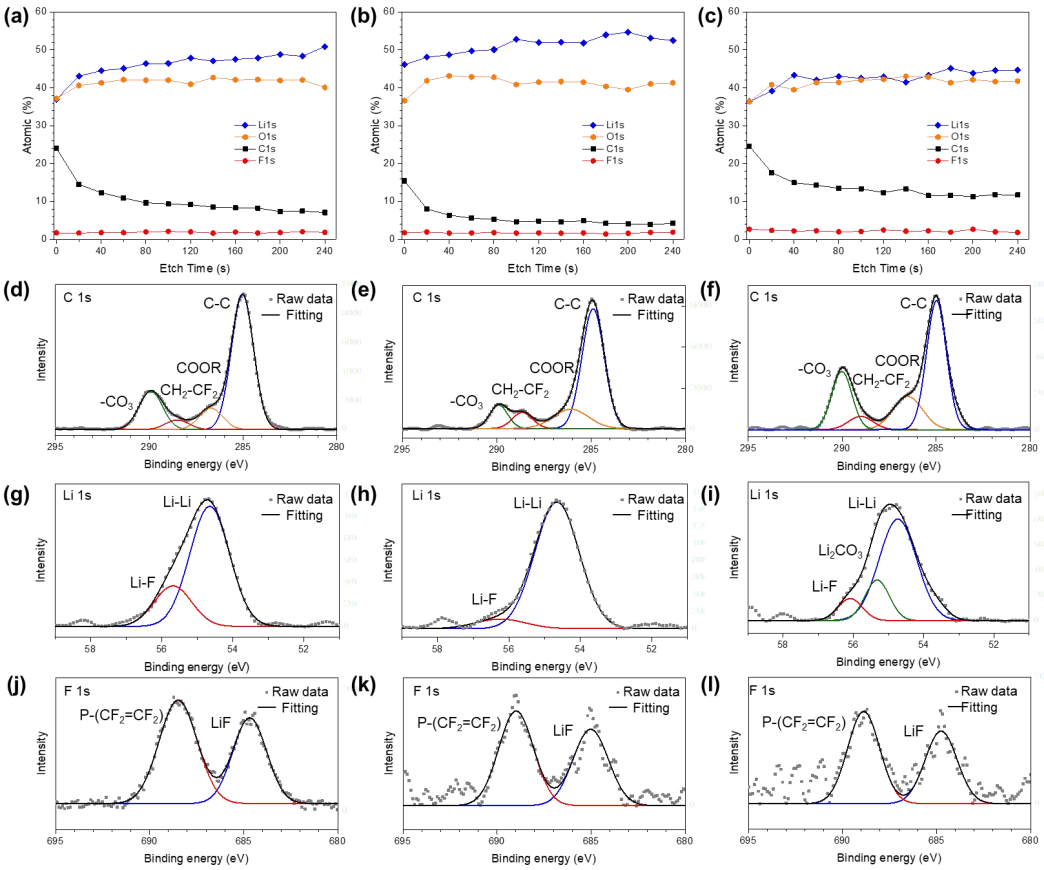

Figure S8. XPS characterizations of anodes after being plated 1 mAh cm^{-2} .XPS depth profile of (a) G-HGA@Li, (b) H-GA@Li and (c)Cu@Li. C 1S spectrum on anodes' surface of (d) G-HGA @Li, (e) H-GA@Li and (f)Cu@Li. O 1S spectrum on anodes' surface of (g) G-HGA @Li, (h) H-GA @Li and (i) Cu@Li. F 1S spectrum on anodes' surface of (j) G-HGA @Li, (k) H-GA @Li and (l) Cu@Li.

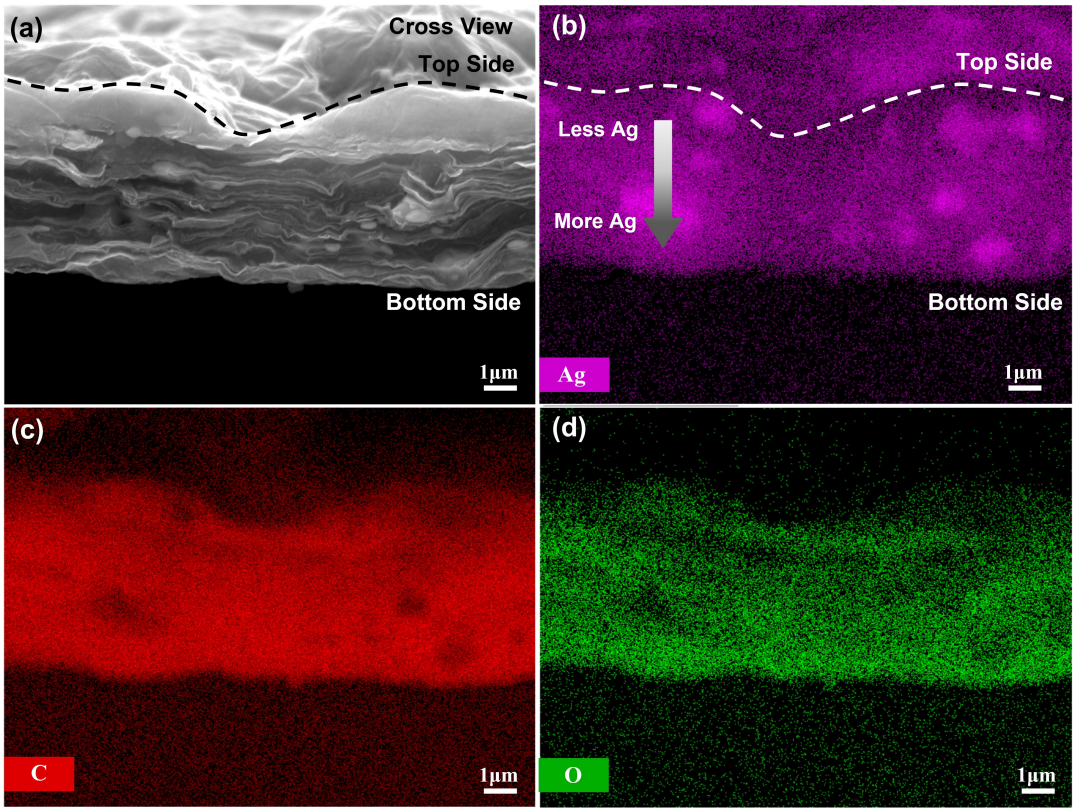

Figure S9. The EDS spectra and element mapping analysis spectra of the G-HGA film. (a)SEM image of G-HGA film;(b-d) EDS element mapping of Ag, C and O elements, respectively.

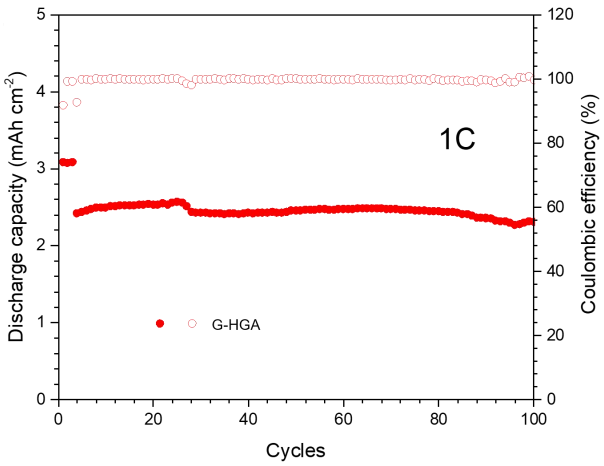

Figure S10. Galvanostatic full cell cycling of G-HGA@Li||LFP (N/P =1.13) at 1C with first three cycles operated at 0.1 C (1 C = 2.65 mAh cm^{-2}).

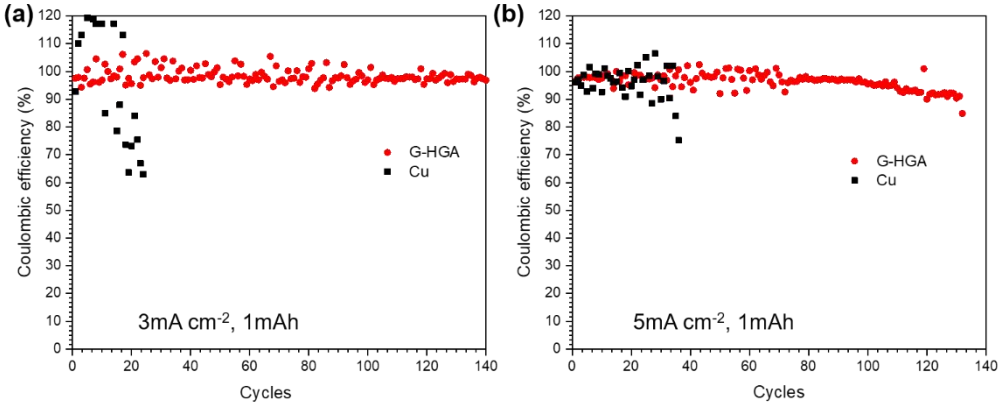

Figure S11. Coulombic efficiency of half cells cycling with G-HGA@Li and Cu@Li at (a) 3 mA cm^{-2}, 1 mAh cm^{-2}, (b) 5 mA cm^{-2}, 1 mAh cm^{-2}.

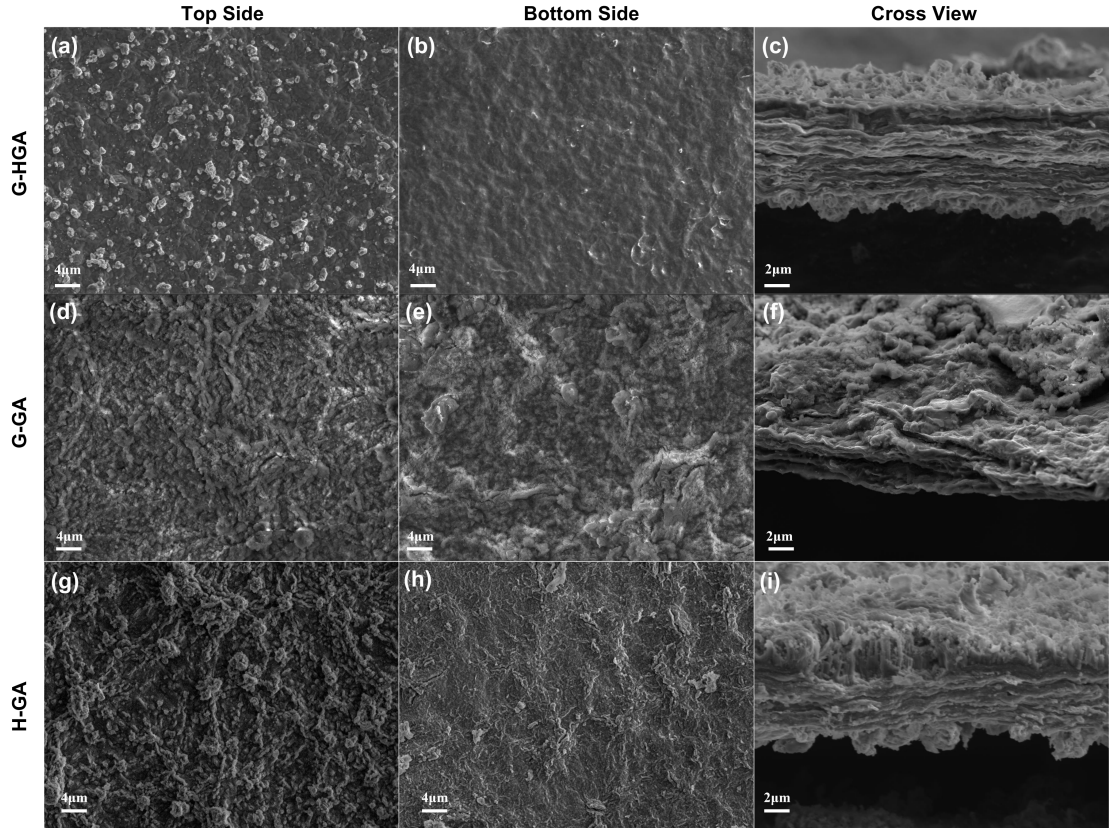

Figure S12. Top view SEM image of (a) G-HGA, (d) G-GA, and (g) H-GA after 50 cycles at 3 mA cm^{-2}. Bottom view SEM image of (b) G-HGA, (e) G-GA, and (h) H-GA after 50 cycles at 3 mA cm^{-2}. Cross view SEM image of c) G-HGA, (f) G-GA, and (i) H-GA after 50 cycles at 3 mA cm^{-2}.

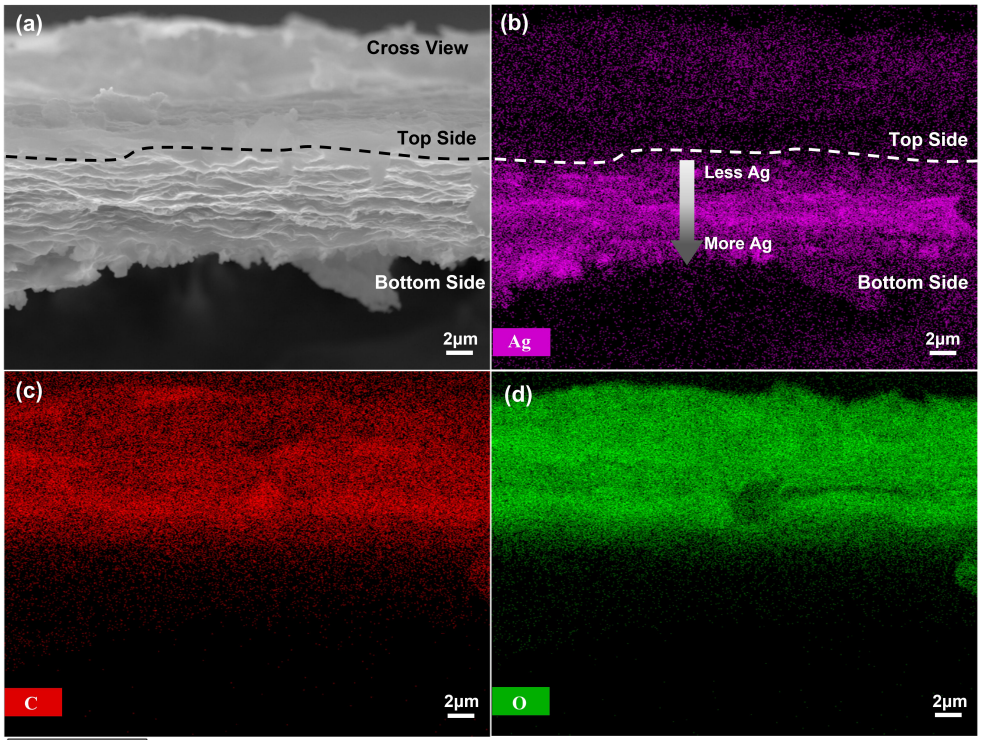

Figure S13. The EDS spectra and element mapping analysis spectra of G-HGA film after 50 cycles at 3 mA cm^{-2}. (a)SEM image of G-HGA film;(b-d) EDS element mapping of Ag, C and O elements, respectively.

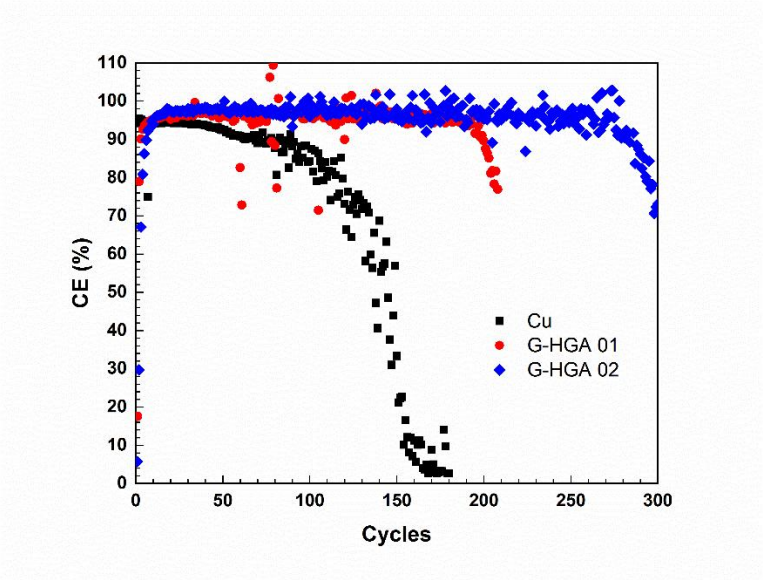

Figure S14. Half cells cycling of bare Cu foil, G-HGA and double-thickness G-HGA

(G-HGA-02) at 1 mA cm^{-2}, 1 mAh cm^{-2} in 1 mol/L $LiFP_6$ in EC/DEC=1:1(v/v) with 10%FEC and 1%VC.